A True Optoelectronic Spectrum Analyzer for Millimeter Waves With Hz Resolution

ANUAR DE JESUS FERNANDEZ OLVERA[ID]**, BENEDIKT LEANDER KRAUSE**[ID]**,
AND SASCHA PREU**[ID]**, (Member, IEEE)**
Terahertz Devices and Systems, Technical University Darmstadt, 64289 Darmstadt, Germany

Corresponding author: Anuar de Jesus Fernandez Olvera (fernandez@imp.tu-darmstadt.de)

ABSTRACT We present an architecture for millimeter-wave spectrum analyzers with Hz resolution and precision based on heterodyne down-conversion using ErAs:InGaAs photoconductive mixers driven by a tunable ultra-narrow linewidth continuous-wave (CW) photonic local oscillator. Unlike previous optoelectronic or electronic architectures, there is no requirement for an external electronic spectrum analyzer or any frequency extenders, keeping the system less complex and less expensive. We demonstrate the architecture for a frequency range that surpasses the E-band range by 10 GHz, i.e. from 50 to 90 GHz, but it is easily extendable to frequencies beyond 300 GHz or to frequencies as low as 25 GHz. A minimum power of 300 fW at 72 GHz was detected when using a resolution bandwidth of 1 Hz.

INDEX TERMS CW photoconductive detectors, ErAs:In(Al)GaAs photoconductors, photomixers, spectrum analyzer, millimeter waves.

I. INTRODUCTION

The emergence of 5G communication networks and automotive radars for autonomous driving has made the development of millimeter-wave systems an industry priority. Development of such systems requires the use of high-resolution measurement equipment for proper characterization, testing and identification of design errors. One of these systems are high-resolution spectrum analyzers that give insight into spectral purity, frequency accuracy, and stability of millimeter-wave emitters, amongst others. Here, we present and experimentally demonstrate, an architecture for a true optoelectronic spectrum analyzer with a Hz-level resolution working in the millimeter-wave range.

To date, two main architectures exist for high-resolution spectrum analyzers working in the millimeter-wave range: a continuous-wave (CW) architecture based on electronic components and a pulsed architecture based on photonic components. The electronic architecture is based on a stand-alone electronic spectrum analyzers (ESAs) that may cover up to 90 GHz [1], or on comparatively 'low' frequency ESAs supplemented with frequency extenders. These frequency extenders are composed of harmonic mixers, and require additional

The associate editor coordinating the review of this manuscript and approving it for publication was Qingli Li[ID].

local oscillators (LOs) to operate [2], [3], however, they can cover frequencies higher than 90 GHz. The additional LOs can be provided by the ESAs, but many of them lack that capability, requiring also the use of external LOs. Hence, the main disadvantage of these electronic architectures is their cost, the difficulty of increasing their frequency coverage, and the scaling of the phase noise for such increased coverage. This is because the harmonic mixers in the frequency extenders use hollow core metallic waveguides with relatively narrow bandwidths (of the order of 50% of its center frequency) [2], [3]. Therefore, large frequency coverage requires many harmonic mixers and the use of relatively high harmonics in the mixing process. The use of many external mixers to cover a certain frequency range increases the complexity of the measurement system, the measurement as a such (requiring the calibration of each individual band [4]) and its cost (even a stand-alone ESA covering up to 90 GHz exceeds by several times the price of a complete photonic CW terahertz system). The use of high harmonics in the mixing process spoils the spectral purity of the spectrum analyzer, given that harmonic mixers basically behave as frequency multipliers, in which the higher the harmonic used, the worse the phase noise performance [5]. Indeed, the use optoelectronic approaches to alleviate this drawback has already been suggested in [5]. The reason is that the phase noise scales as the square of

the harmonic in electronic frequency multipliers [6], contrasting with the nearly constant phase noise scaling of the optoelectronic LO presented here, as we will detail in the next subsections.

The second architecture is based on mode-locked lasers (MLLs) driving pulsed photoconductive mixers [7]–[10]. The pulse generated by the MLL is rectified in the photoconductive mixer resulting in a comb-like structure with a mode spacing given by the repetition rate of the MLL, and a span that extends from DC to several terahertz. If the MLL is sufficiently stabilized, the individual modes of this photonic LO can mix with the signal to be detected to produce a downconverted RF signal susceptible to be analyzed by an ESA. However, it is fundamental to know exactly which mode generated the downconverted RF signal. This can be done by varying the repetition rate of the MLL [8], or by using a dual detection scheme with two photoconductive mixers and a dual-output MLL in which each of the outputs has a different repetition rate [10]. Hence, the main disadvantage of this architecture is the difficulty to analyze wideband signals consisting of several components, because the resulting RF signal will contain several mixing products, as illustrated in [8], [10]. Therefore, it would be necessary to find the exact origin of each of the components to reconstruct the original signal, if possible at all.

Except for the stand-alone ESA in [1] and the photonic version in [10], which is a frequency counter rather than a spectrum analyzer, the implementation of the aforementioned architectures relies on an external ESA, so they are not actually stand-alone spectrum analyzers, but extensions to an existing spectrum analyzer. The architecture presented here, based on the concept introduced in [11], is not an extension, but a true optoelectronic spectrum analyzer in itself capable of analyzing wideband signals composed of several components. It allows for a straight-forward extension to terahertz frequencies without the need of several frequency extenders and with an extremely low phase noise level. The architecture thus combines the advantages of the photonic and electronic realms by using a CW ErAs:InGaAs photoconductive mixer [12] as a wideband heterodyne mixer driven by a tunable photonic LO, and an all-digital intermediate frequency (IF) chain.

The specific details of this new architecture are discussed in Section II. The description of its two possible operation modes are discussed in Section III. The experimental demonstration of both operation modes through the spectral analysis of two different sources emitting around 72 GHz, which corresponds roughly to the center of the covered range, is shown in Section IV. A discussion of the obtained results and a comparison with the results obtained with other architectures are presented in Section V. Concluding remarks are given in Section VI.

II. SPECTRUM ANALYZER ARCHITECTURE
The schematic diagram of the spectrum analyzer architecture is shown in Fig. 1. It can be divided into three subsystems: the

photonic LO subsystem, the heterodyne photomixing subsystem, and the digital IF subsystem. Each of these subsystems will be described in detail in the following subsections.
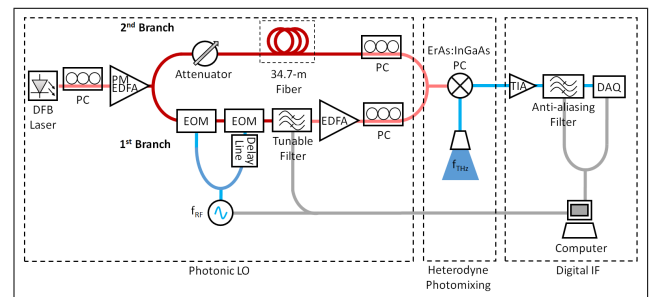

FIGURE 1. Schematic diagram of the implemented spectrum analyzer architecture. The pale red fiber represents non-PM fiber, while the bright red represents PM fiber.

A. PHOTONIC LO SUBSYSTEM
The photonic LO subsystem is composed of a single distributed feedback laser (DFB) whose output is amplified by a polarization-maintaining (PM) erbium-doped fiber amplifier (EDFA). The wavelength and output power of the DFB laser are electronically stabilized and set to 1539.24 nm and 2.5 mW, respectively. Given that the output fiber of the DFB is non-PM, a polarization controller is used to match the output polarization of the DFB to the input polarization of the EDFA. This has to be done only once, and it is achieved by maximizing the power input to the EDFA, given by its built-in power monitor. The EDFA then amplifies the optical signal up to 230 mW. Next, the amplified signal is split into two branches using a PM splitter. The optical signal in the first branch is phase-modulated by two cascaded PM electro-optical phase modulators (EOMs) driven by a computer-controlled CW RF signal generator (Rohde & Schwarz SMP02) with frequency f_{RF} and Hz-level precision. The RF power driving the EOMs is set to 23.5 dBm and 15 dBm, respectively, with no additional DC bias required. This results in a series of sidebands around the main laser mode ($n = 0$) with a separation of f_{RF} between them, as described by the Jacobi-Anger expansion [13]. In order to maximize the number of generated sidebands, the phase of the RF signal driving the two EOMs is adjusted using a wideband tunable RF delay line (LS-0140-KFKM from Spectrum Elektrotechnik). This delay line is adjusted mechanically by monitoring the number and the amplitude of generated sidebands. However, digitally controlled delay lines could allow for an automatic adjustment. Right after the EOMs, an optical tunable band pass filter (XTA-50 from Yenista Optics) selects the mode number n, which is then amplified by a second EDFA. The optical filter is digitally controlled by the same computer controlling the RF generator. Its passband is set to 100 pm (12.7 GHz), and its center frequency digitally selected between 1538.53 nm and 1538.82 nm, depending on the frequency to be generated. Meanwhile, the main optical mode from the DFB laser propagating in the second branch is delayed by 34.7 m of

fiber to compensate for the delay introduced by the filter and the second EDFA in the first branch. By doing this, the coherence between the optical signals propagating in each of the branches is preserved. The amount of fiber required for the compensation was determined beforehand using an in-house developed fiber-based interferometer, but it can also be measured using a commercial optical time-domain reflectometer. Afterwards, the optical power in both branches is equalized by a series of optical attenuators, while the polarization is matched by means of two polarization controllers, one in each branch. Finally, the two branches are combined, resulting in a single optical signal, which is launched to free space using a fiber collimator and then focused onto the photoconductor using a lens, as illustrated in the next subsection. The polarization matching between the two optical branches has to be done only once, and it is achieved by maximizing the photocurrent generated by the optical signal reaching the photoconductive mixer. The power of this optical signal P_{LO} ranges between 14 and 23 mW, depending on the selected mode. Its stability ΔP_{LO}, however, depends mainly on the power stability of the DFB laser and the EDFA, which is better than 0.7 mW overall.
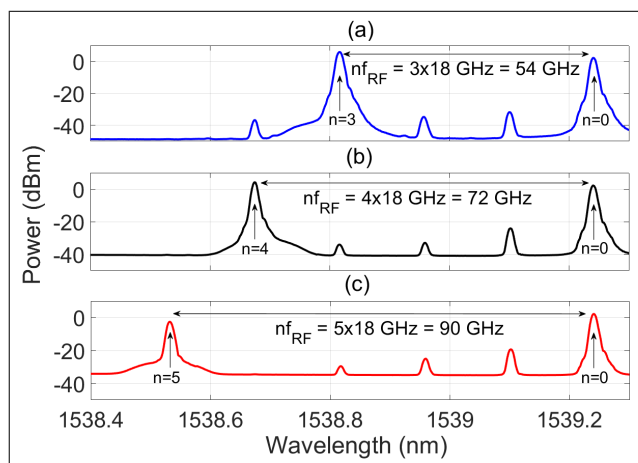

FIGURE 2. Optical spectrum of the photonic LO output for three different configurations: (a) $n = 3$, $f_{RF} = 18$ GHz, (b) $n = 4$, $f_{RF} = 18$ GHz, and (c) $n = 5$, $f_{RF} = 18$ GHz. The shoulders in each of the peaks originate from the side lobes of the DFB laser, but they are suppressed by 30 dB. DFB diodes with >50 dB side lobe suppression are commercially avaialable. The undesired modes appearing periodically are due the finite roll-off of the optical filter. They are suppressed by 27 dB on average. Further or higher order filters would allow for better mode suppression.

The output of this subsystem is then a power-stable photonic signal composed of two coherent modes with an exact frequency separation of nf_{RF}. These optical modes are later transformed into a spectrally pure millimeter-wave LO with the exact frequency given by the difference-frequency generation mechanism of the photoconductive mixer, as we will detail in the next subsection. The determining factor for the extremely high spectral purity of the generated LO is the common origin of the phase noise fluctuations in each the modes. Thus, these fluctuations, coming mostly from the DFB laser, are suppressed by the difference-frequency

generation mechanism of the photoconductive mixer. In this way, the linewidth, stability, accuracy are solely determined by the RF generator without the need for any active stabilization mechanism, even after a change in f_{RF} [14]. More importantly, the linewidth and the frequency stability remain nearly constant as the mode number difference, and hence the frequency, is increased [15], in contrast to what occurs to the phase noise in the harmonic mixers used by electronic frequency extenders. This means that with comparatively simple, table-top RF generators one can already achieve Hz-level resolutions, while locking to frequency standards can allow for better long-term stabilities and increased frequency accuracies [14]. Advanced setups based on atomic clocks or hydrogen masers, with a relative frequency stability in the range of a few 10^{-15} [16], can even allow for a μHz resolution and accuracy, but with a considerable increase in the system complexity.

Sample spectra of the optical output of this subsystem for three different millimeter-wave frequencies are shown in Fig. 2, but certainly, any arbitrary frequency can be generated by just selecting the right combination of n and f_{RF}. This entails changing the center frequency of the filter, changing the frequency of the RF generator and, in some cases, tuning the phase shifter. For this implementation, the maximum measured frequency was 90 GHz, obtained with $n = 5$ and $f_{RF} = 18$ GHz, while the minimum measured frequency was 50 GHz, obtained with $n = 3$ and $f_{RF} = 16.667$ GHz. Smaller frequencies can also be measured. The limit is just set by the minimum separation between sidebands that the filter can still turn into two optical modes with enough side lobe supression, which turns out to be 25 GHz. However, at such low frequencies the performance of the antenna attached to the photoconductive mixer is not optimal, as it will be discussed in the next subsection.

Regarding the measured phase noise performance, the 3-dB linewidth of the generated LO was measured to be less than 1 Hz, and its frequency stability better than 0.33 Hz/s.

In sum, the demonstrated photonic LO had an optimal frequency coverage that ranged between 50 GHz and 90 GHz. Higher frequencies can easily be achieved by adding more cascaded EOMs, using different EOM models, or by mixing positive and negative sideband orders by means of an additional filter, given that the limiting factor is just the amount of generated sidebands. Indeed, similar photonic systems have demonstrated a frequency coverage up to 1 THz [17]. Lower frequencies can be achieved without any further modification on this subsystem, but with a non-optimal performance on the heterodyne downconversion. If optimal performance for lower frequencies is of interest, the antenna of the photoconductive mixer can be re-designed.

B. HETERODYNE PHOTOMIXING SUBSYSTEM
The heterodyne photomixing subsystem is composed of a CW ErAs:InGaAs photoconductor attached to a logarithmic spiral antenna with a maximum radius of 600 μm, and a hyper-hemispherical silicon lens adhered to the 500-μm

thick photoconductor substrate, as shown in Fig. 3. The 10-mm diameter hyper-hemispherical silicon lens, with a hyper-hemisphericity of 1 mm, helps to efficiently couple the incoming millimeter-wave radiation to the logarithmic spiral antenna, which, due to its finite size, has an optimal performance for frequencies above 50 GHz. The performance of such devices as millimeter-wave and terahertz photoconductive detectors is described in detail in [12]. They have been previously employed to detect terahertz signals up to 2.75 THz [18] using well-designed packages like the one shown in [19], underscoring their extreme tunability, frequency coverage, and ease-of-use.
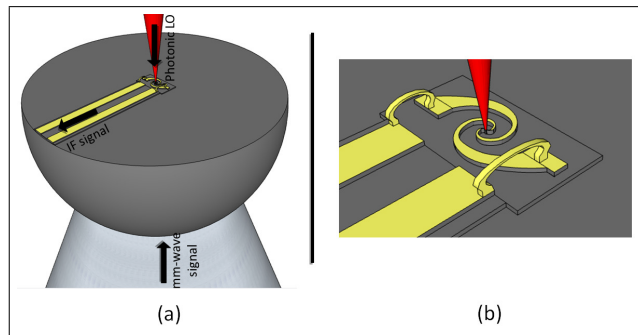

FIGURE 3. (a) Graphical representation of the relationship between the photonic LO subsystem output, the digital IF subsystem input, the millimeter-wave signal (mm-wave) to be analyzed, and the photoconductive mixer of the heterodyne photomixing subsystem. (b) Magnified view of the photoconductive mixer with its attached broadband spiral antenna, and the silicon lens used to in-couple the millimeter-wave radiation.

Their operation as optoelectronic mixers can be described by two distinct mechanisms: the difference-frequency generation mechanism that produces the LO from the photonic signal, and the actual mixing mechanism occurring when a millimeter-wave signal with the right frequency is detected by the antenna attached to the photoconductor.

The difference-frequency generation mechanism has its origin in the absorption process of the photonic LO by the photoconductor, whose electric field strength $E_{LO}(t)$ is given by

$$E_{LO}(t) = E_0 e^{i\omega_0 t + i\phi_0(t)} + E_n e^{i(\omega_0 + \omega_n)t + i\phi_n(t)} \quad (1)$$

where E_0 and E_n are the electric field strengths of the selected optical modes, $\phi_0(t)$ and $\phi_n(t)$ their phases (including their timing jitter due to their phase noise), ω_0 the angular frequency of the main laser mode, and $\omega_n = 2\pi n f_{RF}$. The absorption of the photonic LO generates electron-hole pairs in the photoconductor at a rate proportional to its instantaneous intensity, $I_L(t) \sim E_{LO}(t) \cdot E_{LO}^*(t)$. Thus, the instantaneous photoexcited carrier density $n_{LO}(t)$ is

$$n_{LO}(t) \sim |E_0|^2 + |E_n|^2 + 2|E_n E_0| \cos\left(\omega_n t + \phi_0(t) - \phi_n(t)\right). \quad (2)$$

Although the DFB laser may have a linewidth in the MHz range, resulting in a timing jitter in the order of a few

microseconds, this timing jitter is practically the same for both modes, as explained in the previous subsection. Hence, the difference-frequency generation mechanism removes the jitter from the DFB laser, resulting in $\Delta\phi_n = \phi_0(t) - \phi_n(t)$, which does not possess any explicit time dependence anymore. Therefore, the spectral purity of the photomixed LO is dominated by the spectral purity of the RF generator, not by the linewidth of the DFB laser in contrast to usual CW terahertz systems.

When the millimeter-wave signal to be analyzed, with field $E_{MMW}(t)$, is received by the antenna attached to the photoconductor, the field is transformed into a bias that separates the charges generated by the photonic LO. This results in the mixing of the signals via the emergence of a drift current $i_d \sim n_{LO}(t) E_{MMW}(t)$, which is transmitted through a coplanar stripline to the digital IF subsystem, as shown in Fig. 3. For the specific case of a single-frequency millimeter-wave signal $E_{MMW}(t) = E_{MMW,0} \cos\left(2\pi f_{MMW} t + \phi_{MMW}(t)\right)$, the drift current is primarily composed of three terms: f_{MMW}, $nf_{RF} + f_{MMW}$, and $nf_{RF} - f_{MMW}$. The first two terms are in the millimeter-wave range and thus far beyond the bandwidth of the digital IF subsystem. Only the term $nf_{RF} - f_{MMW}$ may generate a detectable component $i_{det}(t)$, given by

$$i_{det}(t) \sim E_{MMW,0} E_n E_0 \cos\left((\omega_n - \omega_{MMW})t + \phi_{det}(t)\right) \quad (3)$$

where $\phi_{det}(t) = \Delta\phi_n - \phi_{MMW}(t)$. Such component is detected only when $|f_n - f_{MMW}|$ is within the detection bandwidth of the digital IF subsystem. Its amplitude stability is determined by the power stability of the photonic LO, because $E_n E_0 \sim P_{LO}$. If we express the fluctuations in the detected amplitude Δi_{det} originating from the LO fluctuations as

$$\Delta i_{det} = \frac{\Delta P_{LO} E_{MMW,0}}{P_{LO} E_{MMW,0}} = \frac{\Delta P_{LO}}{P_{LO}}, \quad (4)$$

we can estimate that the amplitude fluctuations in the detected current do not exceed -26 dB. Where we have used the previously stated power stability values of the photonic LO.

C. DIGITAL IF SUBSYSTEM

The digital IF subsystem is composed of a transimpedance amplifier (TIA, PDA-S from TEM Messtechnik), a reconfigurable analog anti-aliasing filter (LTC1564 from Linear Technology), and a reconfigurable data acquisition card (DAQ, USB-6210 from National Instruments). The TIA features a gain of 3.3×10^5 V/A, and it is directly connected to the ErAs:InGaAs photoconductive mixer via the coplanar stripline in order to transform the relatively small current $i_{det}(t)$ into a voltage. The anti-aliasing filter, with a reconfigurable cutoff frequency tunable from 10 kHz to 150 kHz in steps of 10 kHz, and the acquisition card, with a maximum sampling frequency of 250 kS/s, are both controlled by the same computer controlling the photonic LO subsystem. The input of the anti-aliasing filter is directly connected to the TIA, and its output connected to the DAQ, which finally digitizes the detected signal.

In principle, the detection bandwidth Δf_{DET} is determined by the sampling frequency of the DAQ, that can be set to any value below 250 kS/s. This would imply a maximum Δf_{DET} of 125 kHz, according to the Nyquist–Shannon theorem. However, this would require an anti-aliasing filter with an extremely sharp response, able to prevent that any signal with a frequency higher than 125 kHz is sampled by the DAQ. Since most analog filters have a rather gradual roll-off, the cutoff frequency of the anti-aliasing filter must actually be chosen lower than the Nyquist-Shannon limit to prevent the leakage of higher frequency signals. Here, we have chosen a factor of approximately 2 lower, a value that guarantees a strong enough attenuation for frequencies above the Nyquist-Shannon limit. Hence, in practice, Δf_{DET} is effectively set by the cutoff frequency of the anti-aliasing filter. A digital low-pass filter with the same cutoff frequency is then used to remove any traces of components with frequencies above the cutoff from the digitized signal.

III. OPERATION MODES

The proposed spectrum analyzer has two possible operation modes, one with a very wide span but a limited resolution bandwidth (RBW) and one with an arbitrarily high RBW but a relatively limited span. In principle, one can use the first mode to locate the signal to be analyzed, and the second mode to perform a precise characterization of its spectral structure. However, the two modes are completely independent of each other and can be used to analyze different kinds of signals. The details of each of them are explained in the next subsections.

A. OPERATION MODE I (WIDE-SPAN MODE)

This mode performs a sweep of the LO and records the square of the detected current at each frequency step, similar to what is done in a classical frequency-swept ESA. Its RBW is equal to $2\Delta f_{DET}$ due to the ambiguity existing between positive and negative frequency differences that can result from the mixing process, i.e. both $f_{LO} - f_{MMW}$ and $f_{MMW} - f_{LO}$ can generate exactly the same detected current regardless of the sign of the difference.

As discussed in the last section Δf_{DET} is determined by the settings of the anti-aliasing filter and the DAQ, having a maximum value of 70 kHz at a sampling frequency of 250 kS/s, and a minimum of 10 kHz at sampling frequency of 40 kS/s. Thus, the RBW can only be tuned from 20 kHz to 140 kHz in steps of 20 kHz. The tuning is done by digitally reconfiguring the anti-aliasing filter cutoff frequency and the DAQ sampling frequency through a graphical user interface in the computer controlling each of the subsystems. The frequency span can be tuned to any range between 50 GHz and 90 GHz by digitally tuning the RF generator frequency, the optical filter, and in some cases, the delay line. The first two parameters are set also through the graphical user interface, while the last one must be tuned mechanically, if required at all. Once the parameters are set, the spectrum analyzer automatically performs the sweep by continuously changing the frequency of the RF frequency generator.

Given that the RBW of this mode is $2\Delta f_{DET}$, the frequency step size of the sweep should be smaller than $2\Delta f_{DET}$ to avoid losing spectral resolution. The smaller the step the size, the more the frequency points, and the more the noise can be reduced through higher order post-detection filters, i.e. video-bandwidth filters (VBW). Additionally, one can also take the average over several samples at each frequency step to increase the sensitivity further. However, this increases the sweep time significantly. If a rather fast and coarse sweep is required, one can also undersample the spectrum by taking step sizes much bigger than $2\Delta f_{DET}$. The minimum sweep time is given by Mt_s, where M is the number of frequency steps, and t_s the settling time of the RF generator after each frequency change, equal to 11 ms for this implementation. No additional stabilization time is required.

B. OPERATION MODE II (HIGH-RESOLUTION MODE)

This operation mode keeps the frequency of the LO fixed, while a time trace of the detected signal is acquired. A Fourier transform then generates the spectrum, similar to ESAs with an all-digital IF chain. The RBW is given by f_s/N, f_s being the sampling frequency of the DAQ, and N the number of acquired points for each measured spectrum. N can be changed at will, allowing an arbitrary RBW within the DAQ specifications. These parameters, as well as the LO frequency, are also set via the graphical user interface in the computer controlling each of the subsystems. In practice, however the RBW limit is determined by the long-term frequency stability of the RF generator of the photonic LO, and by the ambiguity between positive and negative frequency differences. The long term frequency stability of the RF generator imposes a hard limit, which for this implementation is around 1 Hz. The ambiguity in the resolution resulting from the impossibility to distinguish between negative and positive frequency differences is rather a soft limit for this mode. It can be easily overcome by first locating the actual frequency of the signal to be analyzed using the smallest resolution bandwidth of the wide-span mode, and then using this mode with its maximum span. The maximum and minimum span of this mode are determined by the anti-aliasing filter and the DAQ, resulting in a maximum of 70 kHz and a minimum 10 kHz. The tuning is also done in steps of 10 kHz through the graphical user interface. The sweep time is equal to N/f_s.

IV. EXPERIMENTAL DEMONSTRATION

We tested both operation modes using two different sources emitting around 72 GHz, which is roughly at center of the optimal frequency range of the implemented spectrum analyzer. To test operation mode I, we measured the spectrum emitted by a CW terahertz photomixer driven by the pair of DFB lasers described in [20]. To test operation mode II we measured the spectrum of one of the modes composing the terahertz pulse emitted by a pulsed ErAs:In(Al)GaAs photoconductive antenna (PCA) when driven by a mode-locked

laser (MLL) [19]. The results for each of the modes are shown in the first two subsections.

A. DEMONSTRATION OF OPERATION MODE I

Fig. 4 shows the recorded spectrum of the millimeter-wave signal emitted by the CW photomixer when driven by the two DFB lasers whose temperature and current are kept constant to generate a nominal frequency difference of 73.44 GHz. The settings used for this measurement were the following: the frequency of the photonic LO was swept between 71.92 and 72.08 GHz in 70 kHz steps, and at each step an average of 5,000 samples were taken, f_s was set to 250 kHz, the cut-off frequencies of the anti-aliasing and digital filters to 70 kHz, resulting in a RBW of 140 kHz. Additionally, a VBW filter, implemented as a 13th-order moving average filter, was used after the spectrum was acquired, which was composed of 2,286 frequency points, totaling an acquisition time of 10 minutes. As it is evident, the signal is not centered around 73.44 GHz, but around 72.02 GHz. It also drifts over time, as shown by the spectrogram of Fig. 5, recorded also with the implemented spectrum analyzer. Offsets and drifts of this order are indeed expected, as the lasers temperature and current settings are obtained from a look-up table that has no feedback mechanism. We remark that it is possible to halve the number of acquired points, and thus the measurement time, by tuning the LO in frequency steps of 140 kHz. However, this would also have required reducing the order of the VBW filter.
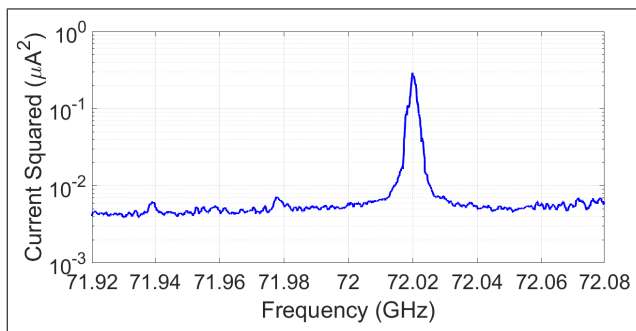

FIGURE 4. Detected current squared reproducing the spectrum of the signal emitted by the CW photomixer. Span: 160 MHz. RBW: 140 kHz.

To determine the sensitivity limits of this operation mode, we varied the power of the millimeter-wave signal by changing the voltage applied to the CW photomixer source while keeping the rest of the measurement settings the same. Afterwards, we measured the emitted power for each of the applied voltages using a PTB (Physikalisch Technische Bundesanstalt)-calibrated pyroelectric detector. The measured results, together with a linear fit, are shown in Fig. 6. The maximum detected power was 130 μW, obtained for the spectrum shown in Fig. 4. Given that the spectral shape for such spectrum was found to be Gaussian with a 3-dB linewidth of 2.86 MHz, the maximum peak spectral density measured with this mode was 40 pW/Hz. The minimum
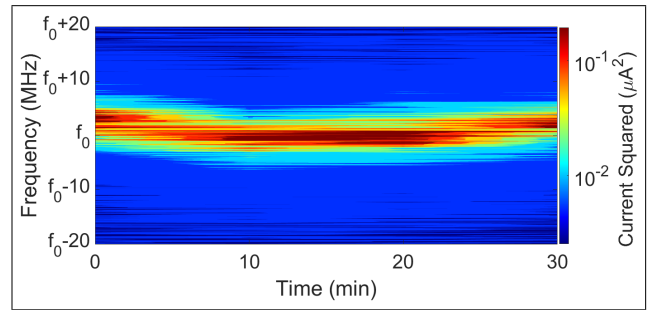

FIGURE 5. Spectrogram of the signal emitted by the CW photomixer. The span was reduced to 40 MHz to highlight the frequency stability of the signal. As pointed out in the main text, f_0 = 72,020 MHz, the center frequency of the emitted signal.
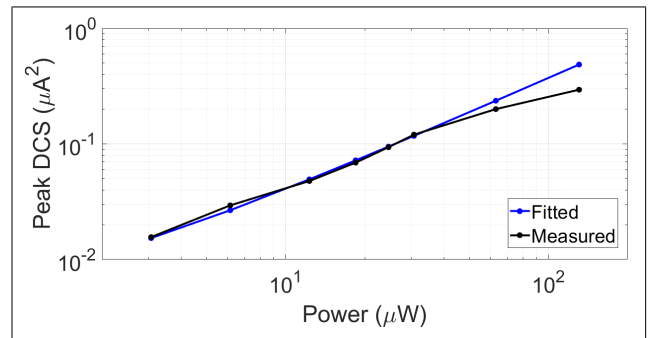

FIGURE 6. Peak of the detected current squared (DCS) as function of incident power originating from the CW photomixer (black) and its linear fit (blue).

detected power was 3 μW, corresponding to a minimum measured peak spectral density of around 980 fW/Hz. There is negligible saturation within the investigated power range, as the comparison with the linear fit shows. The 1 dB compression point is approximately at the highest measured power of 130 μW.

B. DEMONSTRATION OF OPERATION MODE II

Fig. 7 shows the recorded spectrum of the 721st mode of the terahertz pulse emitted by the pulsed ErAs:In(Al)GaAs PCA biased with 200 V and driven by a MLL from Menlo Systems with a nominal repetition rate f_{rep} equal to 100 MHz. The output optical pulse from the MLL had a duration of less than 90 fs, and it was centered around 1560 nm. After photomixing in the PCA, the optical pulse is transformed into a terahertz pulse with the same repetition rate. This terahertz pulse, composed of thousands of modes, is similar to a terahertz frequency comb but with no active stabilization. However, due to the difference-frequency generation mechanism of the photomixing process, there is zero offset as opposed to the phase-envelope offset exhibited by optical combs. In fact, the terahertz pulse can be seen as a modulated signal centered around f_{rep} with an extremely wide modulation bandwidth, as shown in Fig. 8. This means that the actual frequency of each of the emitted modes can be obtained by simply multiplying f_{rep} by the mode number. Thus, the 721st mode should be located around 72.1 GHz.

The settings used in this measurement mode were the following: the frequency of the photonic LO was set to 72.0195167 GHz, f_s to 40 kHz, N to 40,000, and the cut-off frequencies of the anti-aliasing and the digital filters were set to 10 kHz. This resulted in a span of 10 kHz and a RBW of 1 Hz, however, the 1/f noise limited the IF range to 1 kHz-10 kHz, resulting in an effective span of 9 kHz. The acquisition of the spectrum took around 1 s, allowing to monitor the spectrum almost in real time. Although the repetition rate of the MLL was not actively stabilized, it showed negligible drift on the measurement time scale, as shown by the spectrogram of Fig. 9, recorded also with
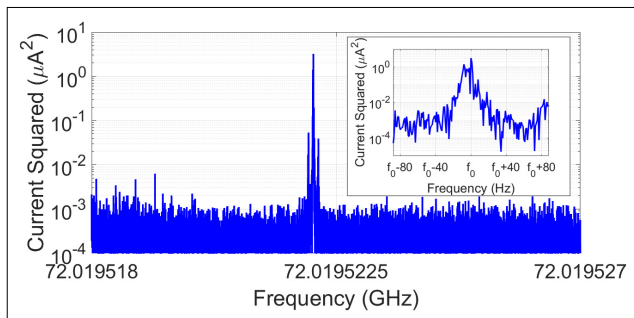

FIGURE 7. Detected current squared reproducing the spectrum of the 721st mode emitted by the pulsed PCA. Span: 9 kHz. RBW: 1 Hz. The inset shows a magnified view of the spectrum centered at $f_0 =$ 72,019,522,083 Hz.
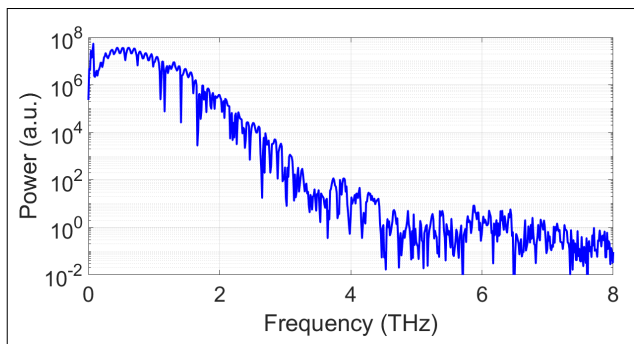

FIGURE 8. Spectrum of the terahertz pulse emitted by the ErAs:In(Al)GaAs PCA as captured by using a TDS system. We remark that this spectrum features the influence of the receiver used in the TDS measurement, and that the TDS frequency resolution is not enough to resolve each of the individual modes composing the terahertz pulse.
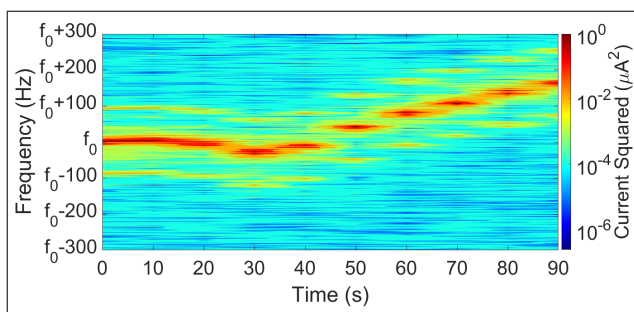

FIGURE 9. Spectrogram of 721st mode emitted by the pulsed PCA. The span was reduced to 600 Hz to highlight the frequency stability of the signal. $f_0 =$ 72,019,522,083 Hz.
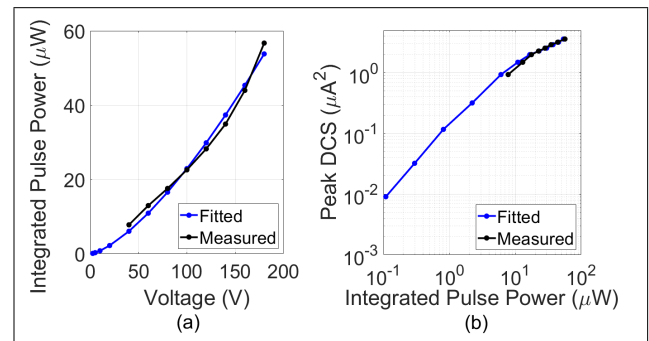

FIGURE 10. (a) Integrated pulse power as a function of applied voltage (black) and its sub-quadratic polynomial fit (blue). (b) Peak DCS as a function of the measured integrated pulse power (black), and as a function of the fitted power (blue).

the implemented spectrum analyzer. The actual frequency of the measured mode shown in Fig. 7 was determined to be 72.019522086 GHz after using operation mode I to resolve for the ambiguity of this mode. This implied an actual repetition rate of 99.888380 MHz, i.e. 111.620 kHz smaller than the nominal repetition rate. The repetition rate of the MLL, simultaneously measured using a photodiode and an external ESA, was indeed 99.888380 MHz, proving the authentic nature of the signal detected by our spectrum analyzer. We remark that due to its extremely broadband nature, this measurement would not have been possible with a MLL-based optoelectronic spectrum analyzer because it would have resulted in a plethora of downconverted modes, making it impossible to determine which of them would actually correspond to the 721st mode without any prior information.

The line shape of the recorded mode was also found to be Gaussian with a 3-dB linewidth of 1.14 Hz, however, such value is the result of the convolution between the LO linewidth and the linewidth of the 721st mode. Given that the LO has also a linewidth close to 1 Hz, the linewidth of the 721st mode is possibly narrower, requiring a higher resolution than the one available for its precise characterization. The two side lobes appearing in the spectrum come from the DFB laser used to generate the photonic LO, and they can be removed by using a laser with higher side lobe suppression ratio. The average power of the emitted pulse, measured with the same PTB-calibrated detector, was 76 μW. This power was distributed over 6.5 THz of bandwidth with a peak around 0.235 THz. According to a theoretical model of the terahertz pulse, the average power in the 721st mode should be on the order of 100 pW.

To determine the sensitivity limits, we again varied the terahertz power by changing the voltage applied to the pulsed PCA source. The results are shown in Fig. 10. The black line in Fig. 10 (a) shows the average power of the emitted pulse measured with the PTB-calibrated pyroelectric detector, which has a noise floor of 1 μW. Hence, in order to obtain the emitted powers below that noise floor, we used a power-law fitting to extrapolate the values at low biases.

Ideally, a PCA would show a quadratic dependence of the emitted power vs. bias. In reality, saturation effects make that dependence subquadratic. Therefore, the fit, represented by the blue line in Fig. 10 (a), resulted in a relationship between integrated pulse power P_{THz} and voltage V given by $P_{THz}(V) = 0.02873\,V^{1.451}$. Fig. 10 (b) shows the estimated detected power of the 721st mode vs. the integrated pulse power. The smallest detected signal was obtained for an applied bias of 2.5 V, corresponding to an estimated power of 300 fW in the 721st mode (the integrated pulse power being 100 nW). Thus, the smallest recorded peak spectral density was smaller than 300 fW/Hz. At integrated pulse powers beyond 10 μW, corresponding to around 30 pW in the 721st mode, we already started seeing saturation.

V. DISCUSSION

The differences between the sensitivity values obtained for operation mode I and operation mode II are attributable to the linewidth and to the structure of the analyzed signal in each case. In particular, the lower power required to saturate the spectrum analyzer in operation mode II is caused by the influence all the other modes composing the emitted pulse, which exhaust a large amount of the photo-excited carriers. We also remark that the power in the 721st mode is an estimate that depends significantly on the assumptions made on its theoretical modelling. The estimations presented so far correspond to a very conservative scenario. The actual noise floor may be substantially lower. If one considers the smallest peak spectral density detected using operation mode I, i.e. 983 fW/Hz, and its associated detection bandwidth, which due to the averaging amounts to around 600 Hz, one could actually predict that it is possible to detect smaller spectral densities than the ones obtained for operation mode II. This is actually expected: the detection limit of ErAs:InGaAs photoconductive mixers has been estimated to be as small as 1.8 fW/Hz when used in coherent detection schemes [12].

Table 1 compares different implementations of existing spectrum analyzer architectures to the one implemented here. Compared to the electronic architecture based on a stand-alone ESA implemented in [1], the main advantage of the CW optoelectronic architecture implemented here is its frequency scalability. It is relatively easy and less expensive to modify the photonic LO to increase its coverage up to 1 THz [17] (by implementing EOMs with larger bandwidth, by using more phase-locked EOMs, or by utilizing the mixing product of positive and negative side lobes through the use of an additional filter), while it would require several frequency extenders to achieve the same frequency coverage with a stand-alone ESA. Compared to the electronic architecture based on frequency extenders [2], [3], the main advantage of this optoelectronic architecture is its superior phase-noise performance. Finally, when compared to implementations based on the MLL-based optoelectronic architecture [8], the two main advantages are the possibility of analyzing wideband signals composed of several frequency tones and the increased sensitivity.

TABLE 1. Comparison between different implementations of the existing millimeter-wave spectrum analyzer architectures.

Architecture Implementation	Nominal Frequency Coverage	Frequency Scalability	Wideband Signal Analysis	Minimum Detectable Power with 1 Hz RBW
Stand-alone ESA [1] (electronic)	**2 Hz-90 GHz**	**Not possible without extenders**	**Possible**	**Not Specified**
VDI frequency extenders [2] (electronic)	**50-90 GHz** (using 2 separate extenders and an external high-end ESA)	**Up to 1,500 GHz** (using 13 separate extenders and an external high-end ESA)[a]	**Possible**	**1 aW**
RPG Radiometer Physics frequency extenders [3] (electronic)	**50-90 GHz** (using 2 separate extenders and an external high-end ESA)	**Up to 500 GHz** (using 8 separate extenders and an external high-end ESA)[a]	**Possible**	**Not specified**
MLL-based [8] (optoelectronic)	**50-1600 GHz** (using an external ESA)	**Not possible**	**Not possible**	**26 nW**[b]
This work (optoelectronic)	**50-90 GHz**	**Up to 1,000 GHz** (using wideband EOMs and an additional optical filter)	**Possible**	**300 fW**[c]

[a]Frequency scaling impaired by phase noise scaling of frequency extenders.
[b]Measured at 99 GHz.
[c]Estimated upper limit at 72 GHz.

From photomixing measurements using similar photoconductive mixers as the one implemented here [12], we can deduce that such sensitivity remains approximately constant up to a frequency of 300 GHz. At higher frequencies, the responsivity starts to decrease due to the carrier lifetime roll-off [21].

Therefore, the proposed spectrum analyzer architecture could be implemented up to 300 GHz with exactly the same performance, and up to terahertz frequencies with a slightly reduced sensitivity.

VI. CONCLUSION AND OUTLOOK

We have shown an optoelectronic free-space spectrum analyzer architecture for the millimeter-wave range. Its Hz-level resolution as well as its tunable frequency coverage were demonstrated by two exemplary measurements of two very different signals both centered around 72 GHz: (i) a signal with a linewidth of 2.86 MHz and a peak spectral density as small as 983 fW/Hz, and (ii) a spectrally purer signal with a linewidth narrower than 1 Hz and an estimated power smaller than 300 fW.

The main advantage of the presented optoelectronic architecture is that it allows the measurement of wideband signals consisting of several frequency modes without the need of acquiring or exchanging multiple millimeter-wave components. This reduces not only the cost, but also the complexity of the measurement process. Additionally, its phase noise performance can outperform the one exhibited by commercially available electronic options, especially for the upper end of the millimeter-wave range.

REFERENCES

[1] R. Schwarz. *R S FSW Signal and Spectrum Analyzer*. [Online]. Available: Accessed: Mar. 21, 2021. [Online]. Available: https://www.rohde-schwarz.com/us/product/fsw-productstartpage_3493-11793.html

[2] V. Diodes. *Spectrum Analyzer Extension Modules Viginia Diodes*. Accessed: Jun. 5, 2021. [Online]. Available: https://www.vadiodes.com/en/products/spectrum-analyzer

[3] RPG-Radiometer Physics. *FS-Z Mixers*. Accessed: Jun. 5, 2021. [Online]. Available: https://www.radiometer-physics.de/products/mmwave-and-terahertz-products/spectrum-analyzer-extenders/fs-z-mixers/

[4] A. Al-Khalidi, K. H. Alharbi, J. Wang, R. Morariu, L. Wang, A. Khalid, J. M. L. Figueiredo, and E. Wasige, "Resonant tunneling diode terahertz sources with up to 1 mW output power in the J-band," *IEEE Trans. THz Sci. Technol.*, vol. 10, no. 2, pp. 150–157, Mar. 2020.

[5] A. Hati, C. W. Nelson, and D. A. Howe, "PM noise measurement at W-band," in *IEEE Trans. Ultrason., Ferroelectr., Freq. Control*, vol. 61, no. 12, pp. 1961–1966, Dec. 2014.

[6] S. Schiller, B. Roth, F. Lewen, O. Ricken, and M. C. Wiedner, "Ultra-narrow-linewidth continuous-wave THz sources based on multiplier chains," *Appl. Phys. B, Lasers Opt.*, vol. 95, pp. 55–61, Apr. 2009.

[7] T. Yasui, R. Nakamura, K. Kawamoto, A. Ihara, Y. Fujimoto, S. Yokoyama, H. Inaba, K. Minoshima, T. Nagatsuma, and T. Araki, "Real-time monitoring of continuous-wave terahertz radiation using a fiber-based, terahertz-comb-referenced spectrum analyzer," *Opt. Exp.*, vol. 17, no. 9, pp. 17034–17043, 2009.

[8] S. Yokoyama, R. Nakamura, M. Nose, T. Araki, and T. Yasui, "Terahertz spectrum analyzer based on a terahertz frequency comb," *Opt. Exp.*, vol. 16, no. 17, pp. 13052–13061, 2008.

[9] N. Wang and M. Jarrahi, "High-precision millimeter-wave frequency determination through plasmonic photomixing," *Opt. Exp.*, vol. 28, no. 16, pp. 24900–24907, 2020.

[10] G. Hu, T. Mizuguchi, X. Zhao, T. Minamikawa, T. Mizuno, Y. Yang, C. Li, M. Bai, Z. Zheng, and T. Yasui, "Measurement of absolute frequency of continuous-wave terahertz radiation in real time using a free-running, dual-wavelength mode-locked, erbium-doped fibre laser," *Sci. Rep.*, vol. 7, Feb. 2017, Art. no. 42082.

[11] S. Preu, "Device and method for spectral analysis," U.S. Patent 0 025 614 A1, Jan. 23, 2020.

[12] A. Fernandez Olvera, A. Roggenbuck, K. Dutzi, N. Vieweg, H. Lu, A. Gossard, and S. Preu, "International system of units (Si) traceable noise-equivalent power and responsivity characterization of continuous wave ErAs: InGaAs photoconductive terahertz detectors," *Photonics*, vol. 6, no. 1, p. 15, Feb. 2019.

[13] E. W. Weisstein. *Jacobi-Anger Expansion MathWorld-A Wolfram Web Resource*. Accessed: Mar. 21, 2021. [Online]. Available: https://mathworld.wolfram.com/Jacobi-AngerExpansion.html

[14] A. R. Criado, C. de Dios, E. Prior, G. H. Döhler, S. Preu, S. Malzer, H. Lu, A. C. Gossard, and P. Acedo, "Continuous-wave sub-THz photonic generation with ultra-narrow linewidth, ultra-high resolution, full frequency range coverage and high long-term frequency stability," *IEEE Trans. THz Sci. Technol.*, vol. 3, no. 4, pp. 461–471, Jul. 2013.

[15] Z. Tong, A. O. Wiberg, E. Myslivets, B. P. Kuo, N. Alic, and S. Radic, "Spectral linewidth preservation in parametric frequency combs seeded by dual pumps," *Opt. Exp.*, vol. 20, no. 16, pp. 1710–1719, 2012.

[16] R. F. C. Vessot, "The atomic hydrogen maser oscillator," *Metrologia*, vol. 42, no. 3, pp. S80–S89, Jun. 2005.

[17] E. Prior, C. de Dios, R. Criado, M. Ortsiefer, P. Meissner, and P. Acedo, "1 THz span optical frequency comb using VCSELs and off the Shelf expansion techniques," in *Proc. Conf. Lasers Electro-Opt. (CLEO)*, San Jose, CA, USA, 2016, Paper SF2O.3, pp. 1–2.

[18] A. D. J. F. Olvera, H. Lu, A. C. Gossard, and S. Preu, "Continuous-wave 1550 nm operated terahertz system using ErAs: In (Al) GaAs photoconductors with 52 dB dynamic range at 1 THz," *Opt. Exp.*, vol. 25, no. 23, pp. 29492–29500, 2017.

[19] U. Nandi, H. Lu, A. C. Gossard, and S. Preu, "ErAs: In (Al) GaAs photoconductor-based time domain system with 4.5 THz single shot bandwidth and emitted terahertz power of 164 μW," *Opt. Lett.*, vol. 45, no. 10, pp. 2812–2815, Nov. 2020.

[20] A. J. Deninger, A. Roggenbuck, S. Schindler, and S. Preu, "2.75 THz tuning with a triple-DFB laser system at 1550 nm and InGaAs photomixers," *J. Infr., Millim., THz Waves*, vol. 36, no. 3, pp. 269–277, 2015.

[21] S. Preu, "A unified derivation of the terahertz spectra generated by photoconductors and diodes," *J. Infr., Millim., THz Waves*, vol. 35, no. 12, pp. 998–1010, Dec. 2014.

ANUAR DE JESUS FERNANDEZ OLVERA received the B.Sc. degree in electronic and computer engineering from Monterrey Institute of Technology and Higher Education (ITESM), Mexico, in 2010, and the M.Sc. degree in electrical engineering from Eindhoven University of Technology (TU/e), Eindhoven, The Netherlands, in 2015. He is currently pursuing the Ph.D. degree with the Terahertz Devices and Systems Laboratory, Technical University Darmstadt, Darmstadt, Germany. His research interests include the development of terahertz systems and applications using photoconductive mixers, as well as their theoretical modeling.

BENEDIKT LEANDER KRAUSE received the B.Sc. degree in electronic and sensor materials from the Technical University Bergakademie Freiberg, Freiberg, Germany, in 2015, and the M.Sc. degree in electrical engineering from Friedrich-Alexander Universität Erlangen-Nürnberg, Erlangen, Germany, in 2019. He is currently pursuing the Ph.D. degree in electrical engineering with the Terahertz Devices and Systems Laboratory, Technical University Darmstadt, Germany. His current research interest includes quasi-optical measurements of terahertz frequencies.

SASCHA PREU (Member, IEEE) received the Diploma degree, in 2005, and the Ph.D. degree *(summa cum laude)* in physics from Friedrich-Alexander Universität Erlangen-Nürnberg, Erlangen, Germany, in 2009. From 2004 to 2010, he was with Max Planck Institute for the Science of Light, Erlangen. From 2010 to 2011, he was with the Department of Materials and Physics, University of Santa Barbara, Santa Barbara, CA, USA. From 2011 to 2014, he worked at the Chair of Applied Physics with Universität Erlangen-Nürnberg. He is currently a Full Professor with the Department of Electrical Engineering and Information Technology, Technical University Darmstadt, Germany, leading the Terahertz Devices and Systems Laboratory. He has authored or coauthored more than 110 journal articles and published conference contributions. His research interests include the development of semiconductor-based terahertz sources and detectors, including photomixers, photoconductors and field-effect transistor rectifiers, and terahertz systems. In 2017, he received an ERC starting grant for developing ultra-broadband, photonic terahertz signal analyzers. He also works on applications of terahertz radiation, in particular, the characterization of novel terahertz components and materials.

• • •